Control over Molecular Architectures of Carbohydrate-Based Block Copolymers for Stretchable Electrical Memory Devices

Chih-Chien Hung,[†] Saki Nakahira,[‖] Yu-Cheng Chiu,[⊥] Takuya Isono,[‖] Hung-Chin Wu,[‡] Kodai Watanabe,[‖] Yun-Chi Chiang,[‡] Shoichi Takashima,[‖] Redouane Borsali,[#] Shih-Huang Tung,*,[†,§] Toshifumi Satoh,*,[‖] and Wen-Chang Chen*,[†,‡,§]

[†]Institute of Polymer Science and Engineering, [‡]Department of Chemical Engineering, and [§]Advanced Research Center for Green Materials Science and Technology, National Taiwan University, Taipei 10617, Taiwan

[‖]Faculty of Engineering and Graduate School of Chemical Sciences and Engineering, Hokkaido University, Sapporo 060-8628, Japan

[⊥]Department of Chemical Engineering, National Taiwan University of Science and Technology, Taipei 10607, Taiwan

[#]CERMAV-CNRS, BP 53, Cedex 9 38041 Grenoble, France

S *Supporting Information*

ABSTRACT: We synthesized a series of new intrinsically stretchable block copolymers (BCPs) in linear AB-type, ABA-type, and star-shaped architectures composed of oligosaccharide (MH) and flexible poly(*n*-butyl acrylate) (PBA) blocks for the application in field-effect transistor memory. The BCP thin films are used as the charge trapping layers in the memory devices where the BCPs phase separate into ordered MH microdomains in soft PBA matrices. The MH microdomain works as the charge-trapping sites while the soft PBA matrix provides a stretchability. In particular, the BCPs of the ABA-type and star-shaped architectures with the end MH blocks not only show superior memory performances but also form

physical networks that impart mechanical resilience to the thin films such that they can endure 100% strain without formation of cracks. The mobilities and the memory windows of the devices are nearly constant even when the charge trapping layers are stretched and released at 50% strain for 1000 cycles. This work highlights the importance of the molecular architectures on the BCPs intended for stretchable electronic materials.
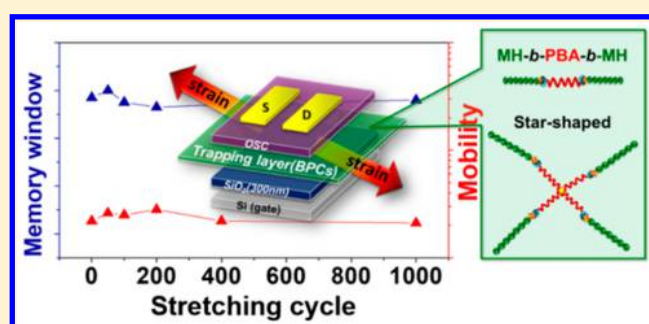
INTRODUCTION

Electronic devices with a high performance as well as a high stretchability are desirable for next-generation applications,[1−7] such as stretchable transistors,[8−14] light-emitting diodes,[15−17] smart sensors,[18−22] memories,[23] and energy-storage devices.[24,25] In the past decade, rapid developments in new materials or concepts for structural design, fabrication techniques, and applications have contributed to the significant progress in the stretchable electronics. Two representative approaches to fabricate stretchable electronic devices have been developed.[26,27] The first method is the manipulation of the geometric structures of nonstretchable materials to be wavy,[2,28] buckled,[5,29−31] or wrinkled.[32] The fattening of such structures under strain prevents the materials from large stress so that the stretchability is enhanced. However, the fabrication processes of this method are complicated and give a low yield. Another approach is the use of intrinsically stretchable components, including stretchable conductor electrodes,[5,12,26,30] dielectrics,[14] and semiconductor materials.[9,11,13,33] This method requires no structural engineering, but the development of the intrinsically stretchable materials suitable for electronic devices is a great challenge.

The synthesis of the intrinsically stretchable block copolymers (BCPs) consisting of conjugated polymer and soft polymer segments has received considerable attention due to their fascinating ordered phase-separated microdomains that can provide desired functions. In our previous work, we have reported the diblock copolymers consisting of carbohydrate (maltoheptaose, MH) and flexible polyisoprene (PI) blocks for stretchable memory applications. MH is a green material and can trap charges.[34−36] We found that various types of memory behaviors, including WORM, Flash, and DRAM, can be created by simply controlling the self-assembled nanostructures of MH-*b*-PIs. Furthermore, the characteristics can be maintained over 500 cycles upon 40% strain due to the introduction of the flexible PI blocks.
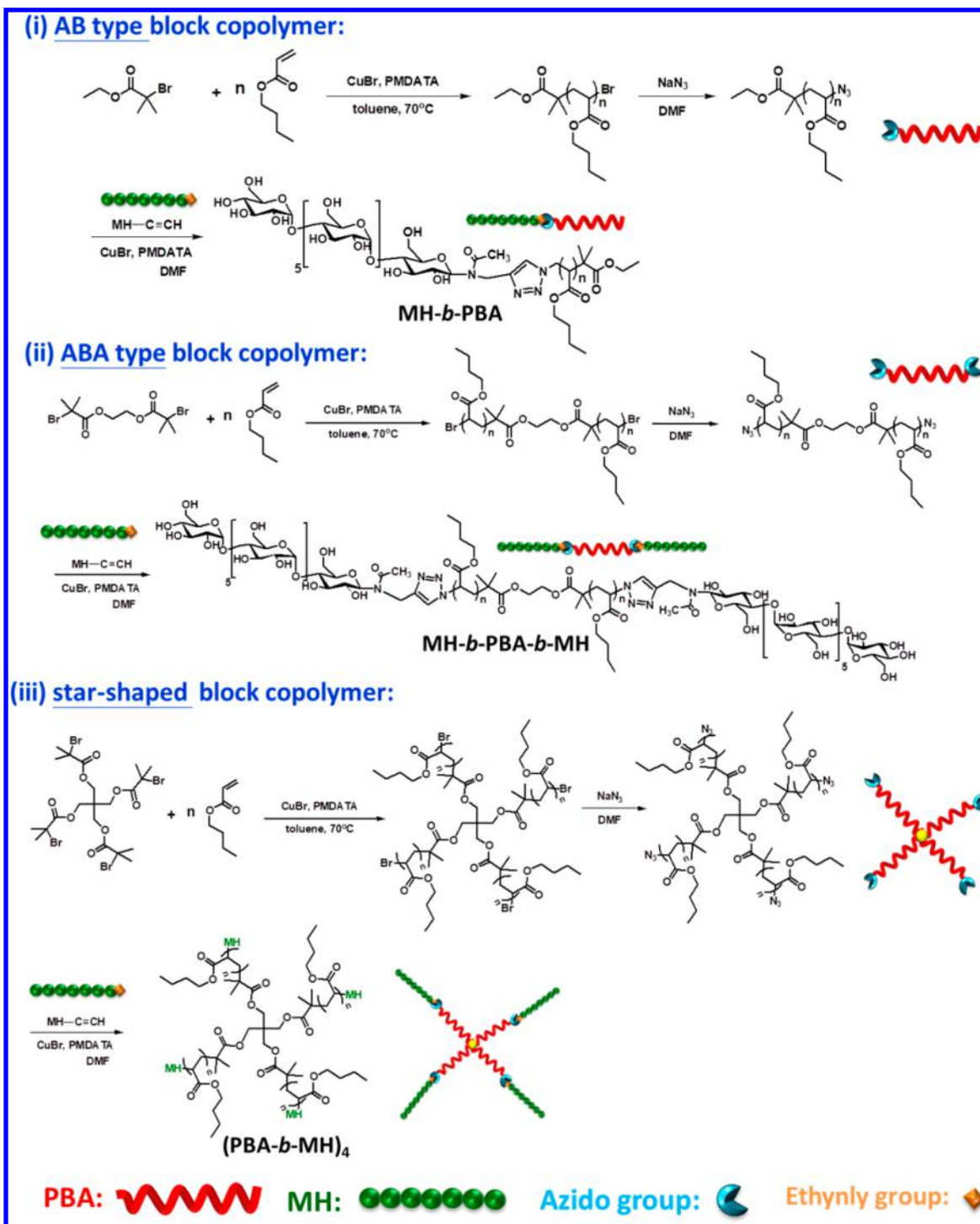
In addition to the typical diblock copolymers, more complicated molecular architectures, such as triblock,[37] multiblock,[38] cyclic,[39] and miktoarm star copolymers,[40,41] have been synthesized. It was shown that more diversified

Scheme 1. Synthesis of AB-Type, ABA-Type, and Star-Shaped Oligosaccharide-Based Block Copolymers

morphologies and mechanical properties can be obtained by altering the molecular architectures of BCPs.[42−45] It would be therefore intriguing to take the advantage of the BCPs bearing soft and electric-responsive segments covalently linked in molecular architectures other than the conventional linear diblock form for the use in stretchable devices and to explore the effects of the molecular architectures on the performance of the devices.

In this work, we synthesized a series of new intrinsically stretchable linear and star-shaped BCPs composed of oligosaccharide (MH) and flexible poly(n-butyl acrylate)

(PBA) blocks by ATRP and click reaction for the application in field-effect transistor (FET) memory. The linear forms include AB-type (MH-b-PBA) and ABA-type (MH-b-PBA-b-MH), and the star-shaped BCP bears four arms with PBA chains in the center, as shown in Scheme 1. The BCP thin films serve as the charge trapping layers in the memory devices where the MH block and PBA block provide charge-trapping capability and stretchability, respectively. We find that the ABA-type and star-shaped BCP thin films show superior memory characteristics that can be stably maintained under a cyclic large stretching, manifesting the critical role of the

molecular architecture. The nanostructures of the BCPs with different molecular architectures were systematically studied by atomic force microscopy (AFM), small-angle X-ray scattering (SAXS and GISAXS), and optical microscopy (OM) to clarify the relationship between the nanostructure, memory characteristics, and stretching behaviors of the BCPs. The mechanical properties were further examined by AFM apparatus operated in the PeakForce tapping mode.

■ RESULTS AND DISCUSSION

Synthesis and Characterization of the Polymers. As outlined in Scheme 1, the AB-type (MH-b-PBA), ABA-type
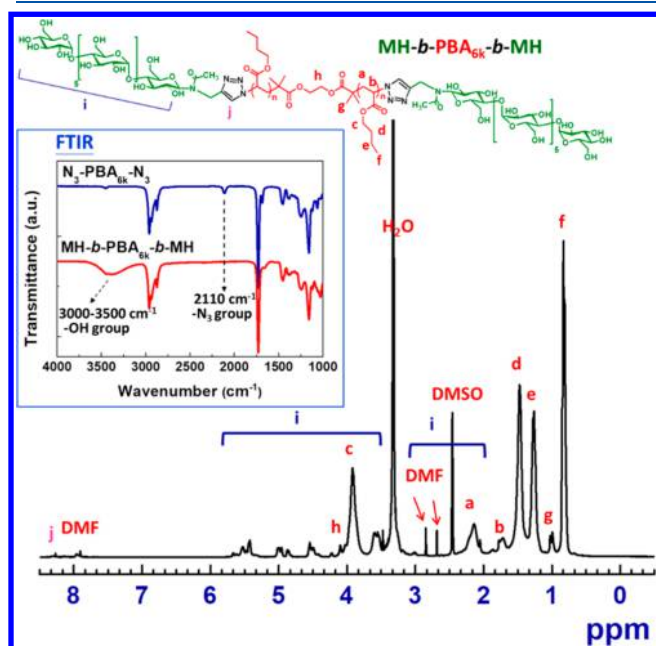
Figure 1. ^{1}H NMR spectrum (400 MHz) of MH-b-PBA$_{6k}$-b-MH and IR spectra of N$_3$-PBA$_{6k}$-N$_3$ and MH-b-PBA$_{6k}$-b-MH.

(MH-b-PBA-b-MH), and star-shaped ((PBA-b-MH)$_4$) BCPs, where MH is A block and PBA is B block, were synthesized. The detailed synthetic procedures are described in the Experimental Section of the Supporting Information. First, the azido-terminated PBAs (PBA-N$_3$, N$_3$-PBA-N$_3$, and (PBA-N$_3$)$_4$) were synthesized via ATRP of n-butyl acrylate using ethyl 2-bromo-2-methylpropanoate, ethylene bis(2-bromoisobutyrate), and pentaerythritol tetrakis(2-bromoisobutyrate) as the initiator, respectively, in which the [monomer]$_0$/[initiator]$_0$ ratios of 100−400 with various reaction times were applied to produce the polymers with different molecular weights. The ^{1}H NMR and FTIR spectra of the azido-
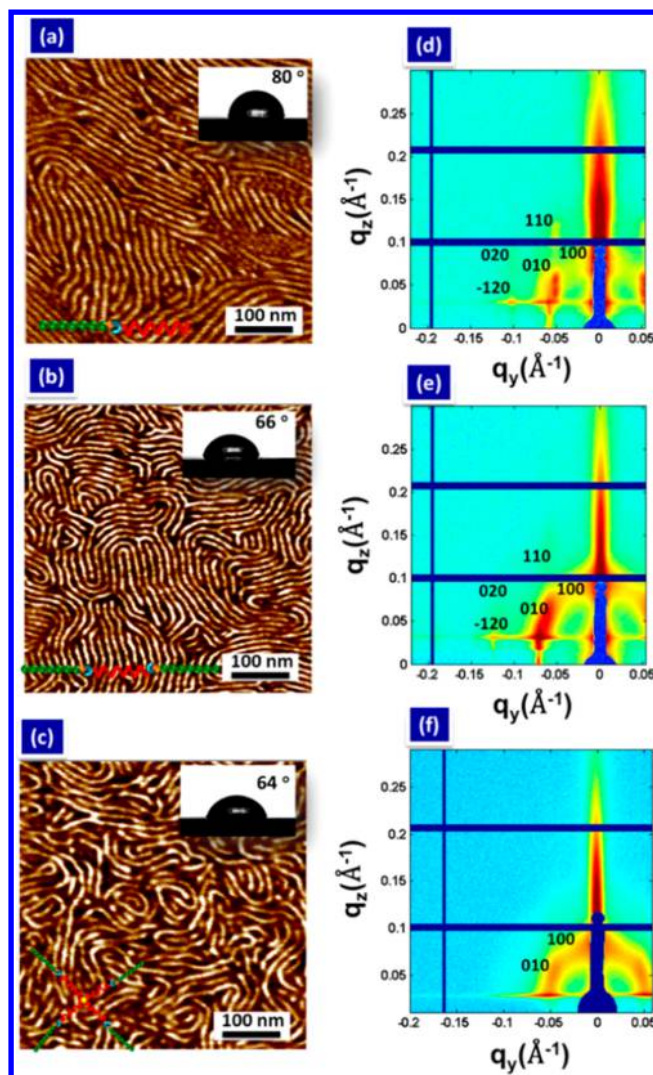
Figure 2. AFM topographies of annealed (a) A1, (b) B1, and (c) C1 thin films. The z scale is 15 nm. 2-D GISAXS patterns of (d) A1, (e) B1, and (f) C1 thin films.

terminated PBAs are shown in Figures S1−S7 of the Supporting Information, which confirm the successful syntheses of these compounds. All the SEC traces exhibit a unimodal elution peak with the M_w/M_n values of 1.12−1.23 (Figures S13−S15). The characteristics of the azido-terminated PBAs are detailed in Table S1.

The azido-terminated PBAs were then covalently linked with N-maltoheptaosyl-3-acetamido-1-propyne (MH−C≡CH) to form block copolymers by click reaction. A representative ^{1}H NMR spectrum from MH-b-PBA$_{6k}$-b-MH is shown in Figure 1,

Table 1. Molecular Parameters and Bulk Strucures of the Block Copolymers

code	sample	f_{PBA}[a]	$M_{n,SEC}$[b] (g/mol)	N_{PBA}[c]	$M_{n,NMR}$ (g/mol)	M_w/M_n[b]	bulk structure[d]	d-spacing[d] (nm)
A1	MH-b-PBA$_{3k}$	0.80	10 100	25	4 430	1.18	HEX cylinder	12.7
A2	MH-b-PBA$_{7k}$	0.88	12 500	52	7 830	1.18	HEX cylinder	13.8
B1	MH-b-PBA$_{6k}$-b-MH	0.78	15 400	46	7 200	1.16	HEX cylinder	10.4
B2	MH-b-PBA$_{10k}$-b-MH	0.86	20 500	82	11 800	1.17	HEX cylinder	12.4
C1	(PBA$_{3k}$-b-MH)$_4$	0.79	31 600	92	13 100	1.18	HEX cylinder	11.3
C2	(PBA$_{5k}$-b-MH)$_4$	0.86	35 600	156	21 300	1.16	HEX cylinder	11.9

^{a}Volume fraction of PBA block (f_{PBA}) was calculated using d_{MH} = 1.36 g/cm^3 and d_{PBA} = 0.90 g/cm^3. ^{b}Estimated by SEC in DMF containing 0.01 mol L^{-1} LiCl using polystyrene standard. ^{c}Degree of polymerization of PBA block. ^{d}Bulk structure and d-spacing determined by SAXS.

Table 2. Thin Film Structures and Memory Characteristics of the Block Copolymers

code	thin film structure[a]	d-spacing[b] (nm)	mobility (cm² V⁻¹ s⁻¹)	$I_{on}/I_{off,av}$	$V_{th,writing}$ (V)	$V_{th,erasing}$ (V)	ΔV_{th}
A1	parallel HEX cylinder	10.1	0.16	4.2×10^6	10	−26	36
A2	BCC sphere	10.9	0.13	5.1×10^6	4	−25	29
B1	parallel HEX cylinder	9.1	0.42	1.3×10^7	42	−25	67
B2	parallel HEX cylinder	9.7	0.31	1.8×10^7	5	−27	32
C1	parallel HEX cylinder	12.7	0.44	7.8×10^6	57	−21	78
C2	parallel HEX cylinder	13.0	0.26	1.6×10^6	23	−23	46

[a]Thin film morphology determined by GISAXS and AFM at 25 °C. [b]Determined from the first-order diffraction peak of GISAXS profiles.
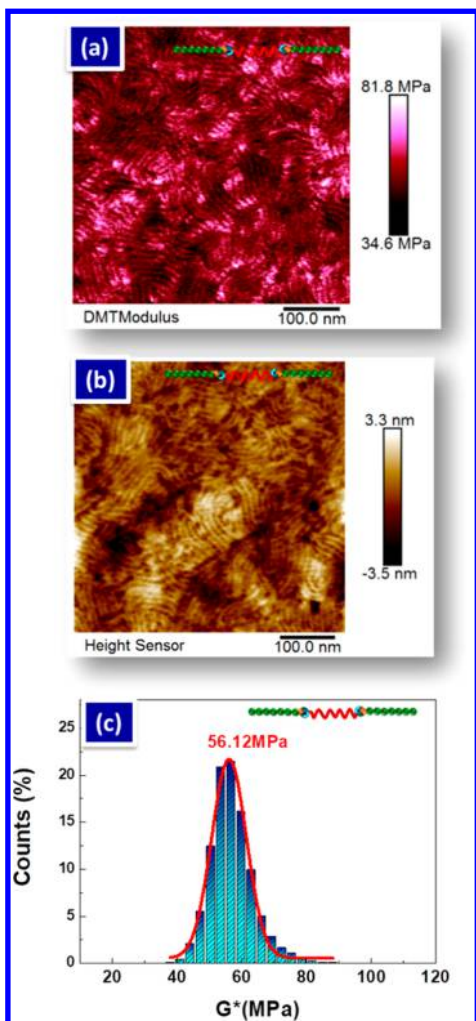

Figure 3. (a) Elastic modulus image, (b) AFM topography image, and (c) distribution of the elastic modulus (E_s) of B1 thin film.
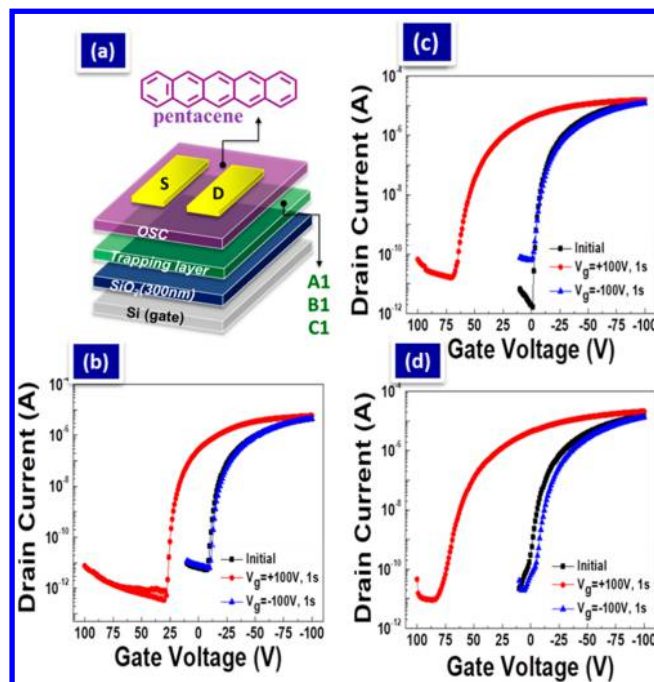

Figure 4. (a) Schematic of the FET memory device. Transfer characteristics of FET memory devices using (b) A1, (c) B1, and (d) C1 thin films as charge trapping layers.

which confirms the presence of the characteristic protons of both the PBA (peak c) and MH (peak i) blocks together with the characteristic signal at $\delta = 8.26$ from the methine proton of the triazole ring (peak j). The corresponding FTIR spectrum in the inset of Figure 1 exhibits a broad absorption peak around 3000−3500 cm⁻¹ resulting from the hydroxyl groups of the MH block, while the absorption peak at 2110 cm⁻¹ from the azido group of N₃-PBA-N₃ disappears. The SEC trace of MH-b-PBA$_{6k}$-b-MH (Figure S14a) exhibits a unimodal peak with the M_w/M_n value of 1.16, which clearly shifts toward higher molar mass as compared to the corresponding azido-terminated PBA precursor. All the BCPs exhibit similar ¹H NMR, FTIR, and SEC results, as shown in Figures S8−S15. The volume fractions of the PBA block (f_{PBA}) for the BCPs

calculated using the reported density values for amylose (1.36 g cm⁻³) and PBA (0.90 g cm⁻³) are in the range 0.78−0.88. The molecular characteristics of the BCPs are listed in Table 1.

Microphase-Separated Structures. The self-assembled structures of the AB-type, ABA-type, and star-shaped BCPs were first investigated by the SAXS technique. The bulk samples were cast from the THF solutions, a poor solvent for MH block, and then solvent-annealed under the vapor of the mixed solvents with THF/H₂O = 1:1 (w/w) for 12 h. The SAXS profiles of the as-cast and annealed samples are compared in Figure S16. The AB-type BCP, MH-b-PBA$_{3k}$ (A1, $f_{PBA} = 0.80$), after annealing exhibits a distinct primary scattering peak q^* with higher order scattering peaks at $\sqrt{3}q^*$, $2q^*$, $\sqrt{7}q^*$, and $3q^*$, indicating that the minor component MH forms a highly ordered array of hexagonal close-packed (HEX) cylinders. Although the diffraction peaks of MH-b-PBA$_{7k}$ (A2, $f_{PBA} = 0.88$) are in order of q^* and $\sqrt{3}q^*$, characteristic of HEX cylinders, the peaks are broader and the higher-order peaks are missing (Figure S16b). This implies a less ordered structure in A2 sample, possibly in the transition state between cylindrical and spherical domains due to the higher fraction of PBA. All the ABA-type and star-shaped BCPs, MH-b-PBA$_{6k}$-b-MH (B1, $f_{PBA} = 0.78$), MH-b-PBA$_{10k}$-b-MH (B2, $f_{PBA} = 0.86$), (PBA$_{3k}$-b-MH)₄ (C1, $f_{PBA} = 0.79$), and (PBA$_{5k}$-b-MH)₄ (C2, $f_{PBA} = 0.86$) show characteristics of HEX
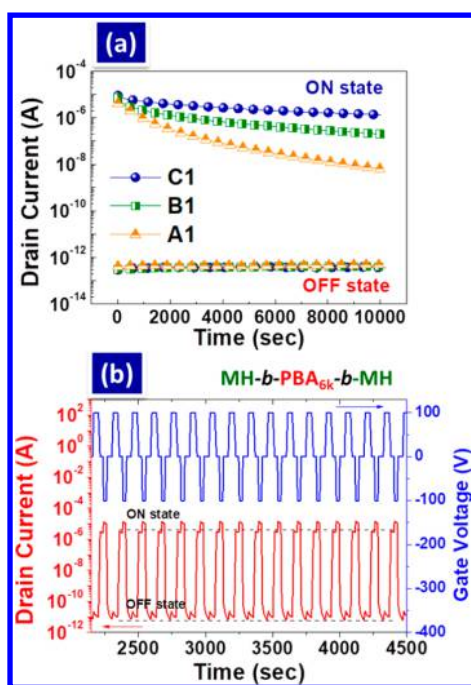
Figure 5. (a) Retention time of A1-, B1-, and C1-based FET memory devices. (b) Endurance characteristic of B1-based FET memory device.

cylinders, among which the star-shaped BCPs are less ordered even after annealing. The d-spacings determined by the relation $d = 2\pi/q$ from the first-order peaks are in the range between 10.4 and 13.8 nm. The bulk morphology and the d-spacings of the studied BCPs are summarized in Table 1. Note that the upper f_{PBA} bound (~0.9) for the HEX cylindrical structure of the BCPs composed of MH and PBA blocks is higher than that for conventional BCPs with both flexible blocks.[46] This is attributed to the high incompatibility between MH and PBA blocks as well as the rigid and extended MH chains that cause the BCPs to preferably microphase separate into domains with a lower curvature to reduce interfacial free energy.

We then examined the morphology in thin films where the confinement effect from the interfaces may orientate the microdomains or even change the structures. The thin films with thicknesses of 50−55 nm were prepared by spin-coating from THF solutions onto bare silicon wafer and solvent-annealed for 12 h. The surface structure of the thin films was characterized by AFM, as shown in Figure 2 and Figure S17. In Figure 2a, the A1 film exhibits a fingerprint-like pattern. In comparison with the SAXS data, the curved stripes are the cylindrical domains parallel to the surface. For the A2 thin film, instead of cylinders, an ordered dot pattern can be clearly seen on the surface (Figure S17d). According to the SAXS data that suggest a transition state for the bulk A2 sample, the dots on the A2 film should be the spherical MH domains that form due to the surface effect. All the ABA-type and star-shaped BCP thin films show parallel cylinders after 12 h annealing, consistent with the SAXS results.

To gain more insights into the morphology and micro-domain orientation, the thin films were subsequently analyzed using GISAXS techniques. The as-cast BCP thin films show ring-like diffraction patterns (Figure S18), indicating that MH microdomains are randomly oriented before annealing. After annealing, A1 exhibits a diffraction pattern characteristic of
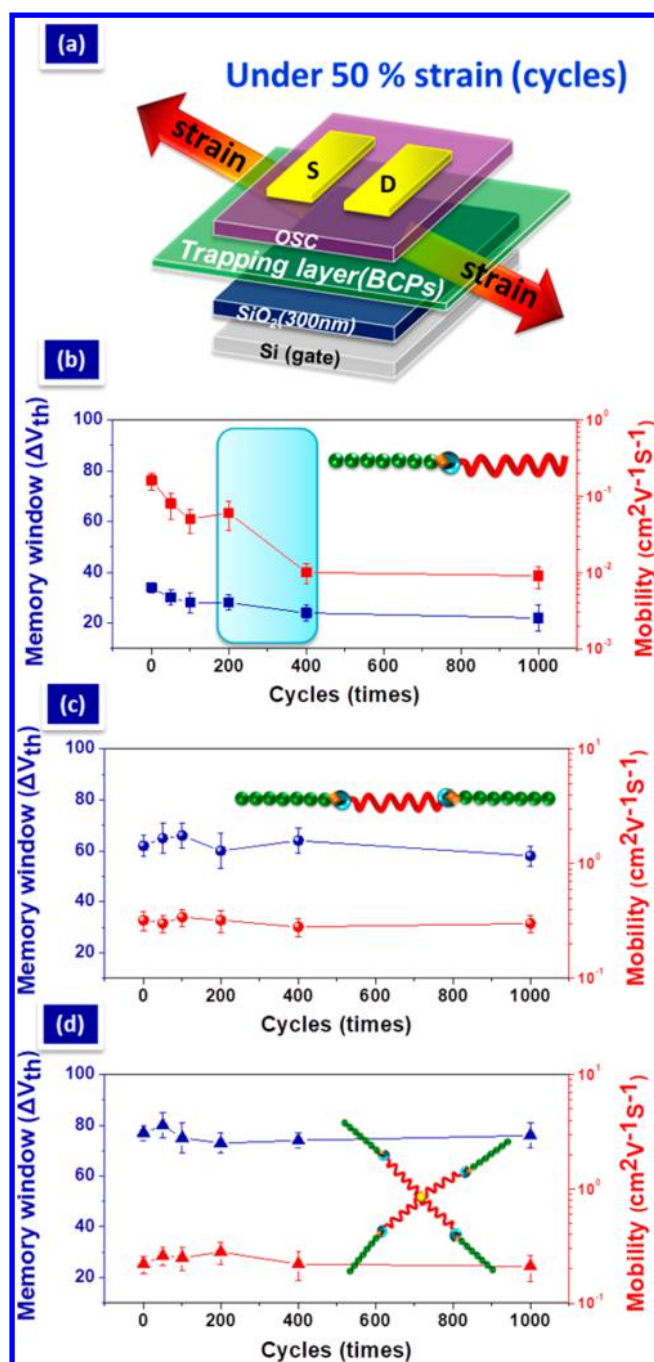
Figure 6. (a) Schematic of the FET memory device under cycling stretching test. Stability of the memory devices with (b) A1, (c) B1, and (d) C1 electret films under cyclic stretching at 50% strain.

HEX cylinders parallel to the surface. The corresponding crystallographic planes are marked in Figure 2d. For the A2 thin film with higher f_{PBA}, GISAXS shows the diffraction pattern of spheres in body-centered cubic (BCC) arrangement, consistent with the spherical domains observed by AFM (Figure S17d). The GISAXS patterns of ABA-type and star-shaped BCP thin films are shown in Figures 2e,f and Figures S17e,f. All reveal parallel HEX cylinders in the thin films. The more diffuse diffraction patterns indicate the microdomains are not as oriented as those in the AB-type thin films. The thin film morphologies of the BCPs are summarized in Table 2.
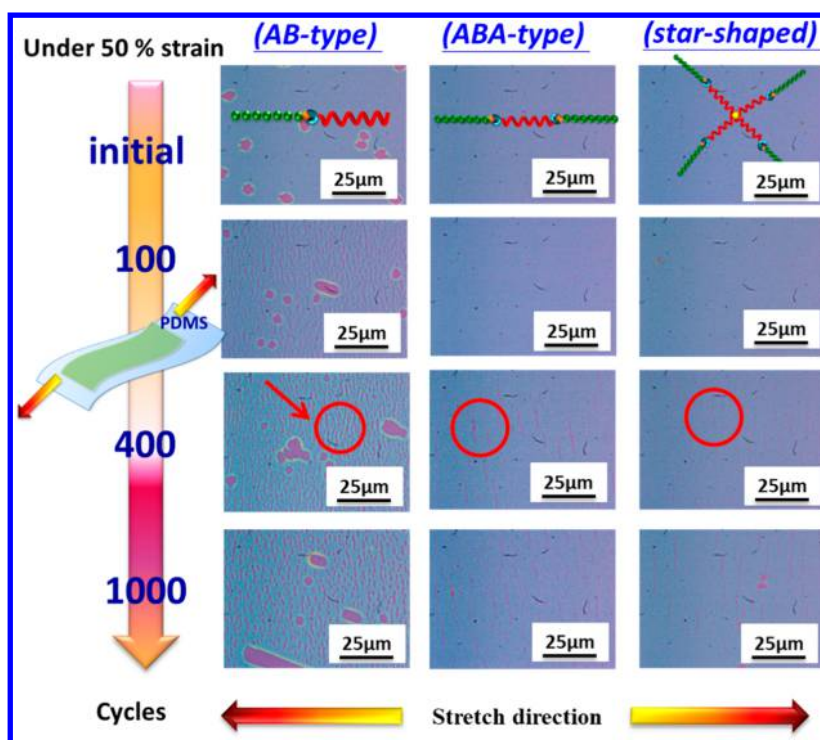
Figure 7. OM images of A1, B1, and C1 thin films under cyclic stretching at 50% strain.
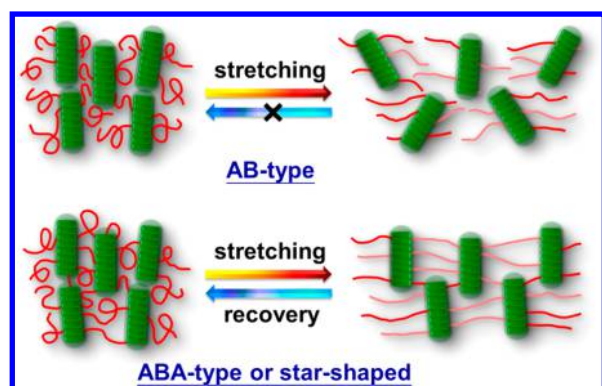

Figure 8. Illustration of the structure changes in AB-type, ABA-type, and star-shaped block copolymers under stretching and releasing.

Mechanical Characteristics. The T_g of PBA is around −54 °C so that the soft PBA block not only serves as an insulator matrix but also provides the stretchable characteristic. To examine the stretchability of the BCP thin films, the films were first transferred onto a polydimethylsiloxane (PDMS) substrate (20:1 mass ratio of base to cross-linker) and then stretched at 100% strain. The morphologies of the films upon strain were investigated by the optical microscopy (OM), as shown in Figure S19. No cracks are observed for B1 and C1 thin films while A1 thin film shows slight cracks under 100% strain even though f_{PBAs} are similar (0.78−0.80). The ABA-type and star-shaped BCPs are apparently more stretchable than the AB-type, suggesting that the molecular architectures can significantly affect the mechanical properties. In the case of the films with higher PBA volume fractions, A2, B2, and C2, all the films remain smooth under 100% strain. The longer flexible PBA chains bring about more entanglements that can effectively hold polymer chains together to prevent fracture.

The mechanical properties of the BCPs thin films were further measured using PeakForce Quantitative Nanomechanical Mapping (QNM). The surface mechanical mapping of the representative ABA-type B1 thin film is shown in Figure 3a where the z-axis represents the elastic modulus. The fingerprint-like pattern is well correspondent with the AFM topography image (Figure 3b), clearly revealing the PBA (soft) and MH (hard) domains with highly distinguishable moduli. Figure 3c shows the distribution of the elastic modulus E_s extracted from Figure 3b, and the averaged elastic modulus is 56.12 MPa. The averaged elastic moduli of all the BCPs are summarized in Table S2, and the values are in the range between 5 and 100 MPa, which is close to the values of rubbers (10−100 MPa) as shown in Figure S20. Moreover, for the BCPs with similar PBA fraction, the averaged elastic modulus is in order of star-shaped > ABA-type > AB-type. Therefore, the flexibility of BCP thin films can be tuned not only by introducing different fractions of soft segments into BCPs but also by designing different molecular architectures.

Electrical Characteristics of FET Memory Devices. The memory characteristics of the prepared FET memory devices using MH-b-PBA$_n$, MH-b-PBA$_n$-b-MH, and (PBA$_n$-b-MH)$_4$ as the electrets were investigated. Here the electrets also serve as the charge storage layers. The devices were fabricated in the bottom-gate/top-contact configuration with p-type semiconductor pentacene as charge transport layer, as shown in Figure 4a. The measurements were conducted in dark to prevent the light-induced charge transfer or excitons. Figures 4b−d show the representative transfer curves for A1, B1, and C1 thin films, all of which exhibit the typical p-type accumulation mode with good current modulation. The field-effect mobilities measured in the saturation region of the devices using A1, A2, B1, B2, C1, and C2 thin films as electrets are 0.16, 0.13, 0.42, 0.31, 0.44, and 0.26 cm^2 V^{-1} s^{-1}, respectively, and the I_{on}/I_{off} ratios are 10^6−10^7.

To switch the conductance of transistor-type memory devices, the charges should be stored in or released from the electret layers in a controlled manner. The devices were applied with a gate pulse ±100 V for 1 s to achieve the charge storage and release state, i.e., ON and OFF state, of the memory devices. When a positive gate bias $V_g = +100$ V is applied for 1 s, a positive shift is observed on the transfer curve, which is caused by the injection of the induced electrons from the pentacene layer into the electret layer. This operation is defined as the "writing" process. On the contrary, a negative gate bias $V_g = -100$ V for 1 s drives the holes to inject into the electret and leads to a negative shifting of transfer curve, known as the "erasing" process. The capacity of digital information storage, called memory window, is defined as the threshold voltage difference between writing and erasing state. Figures 4b−d show the positive and negative shifts of the transfer curves of the memory devices at a fixed drain voltage V_d of −80 V for A1, B1, and C1 electrets, and the memory characteristics for all the samples are listed in Table 2. The memory windows of the devices using A1, A2, B1, B2, C1, and C2 as charge storage electret layers are 36, 29, 67, 32, 78, and 46 V, respectively. The memory capacity is significantly improved as the fraction of the MH moiety increases. This is because the MH moiety can effectively trap electrons through the deprotonation on hydroxyl groups.[35] Interestingly, although the morphologies and MH fractions of the AB-type (A1, $f_{MH} = 0.2$), ABA-type (B1, $f_{MH} = 0.22$), and star-shaped BCP electrets (C1, $f_{MH} = 0.21$) are similar, C1-based device shows the largest memory window, followed by B1-based device. A similar result is found when comparing A2 ($f_{MH} = 0.12$), B2 ($f_{MH} = 0.14$), and C2 ($f_{MH} = 0.14$) electrets. Therefore, in addition to the MH fraction, the molecular architecture of the BCPs is another factor that affects the memory performance and the memory window can be greatly expanded by increasing the number of MH blocks in the BCPs.

The long-term stability of the trapped charges in the BCP electrets was examined, and the drain current as a function of time is exhibited in Figure 5a. The retention time is defined as the time duration of the stored charges retained in the charge storage layer. The currents of the ON and OFF states for the B1- and C1-based devices can be well maintained for at least 10^4 s with I_{ON}/I_{OFF} ratios above 10^6, among which the C1 electret is particularly stable. In contrast, when using A1 as the trapping layer, the current of the ON state decreases by 3 orders of magnitude in the same period, with a I_{ON}/I_{OFF} ratio down to 10^4, indicating a poor retention time for the AB-type BCP electrets. Again, both the molecular architecture of the BCP and the fraction of MH can significantly affect the long-term stability of OFET memory devices. The ON/OFF state switching endurance of the devices with B1 thin film was evaluated by the writing/reading/erasing/reading (WRER) cycle measurement. The drain current was kept at $V_d = -80$ V, and the writing, reading, and erasing processes were implemented at $V_g = 100$, 0, and −100 V, respectively. The results in Figure 5b indicate that the memory device using B1 as the electrets can achieve an I_{ON}/I_{OFF} ratio around 10^6 over 100 cycles.

For AB-type BCPs, each PBA block has one chain end that prefers to locate at the interfaces to lower the surface free energy.[47,48] Considering the molecular architectures of the ABA-type and star-shaped BCPs, the PBA chains are in the middle between end MH blocks. The tendency of PBA to locate at interfaces is thus lower because PBA no long has

chain ends to play such a role. In other words, the contact area of MH phase with pentacene at the interface should be larger for ABA-type and star-shaped BCPs even though the MH factions are similar. The water contact angle analysis displayed in Figure 2 demonstrates that the contact angles (66° and 64°) of B1 and C1 thin films are lower than that of A1 film (80°), confirming a greater number of hydrophilic MH segments on the surface for ABA-type and star-shaped BCPs. It has been shown that a higher contact area between the charge trapping sites and the semiconductor layers can enhance the memory performance.[34] This explains why the performances of the devices using ABA-type and star-shaped BCPs as electrets are generally superior to those with AB-type BCP.

Stretchable FET Memory. The memory characteristics of the devices using the BCPs as the charge trapping layer upon stretching were further examined. The BCP thin films were stretched on PDMS substrates and then transferred onto SiO_2/Si substrates for FET device fabrication, as shown in Figure S21. We measured the transfer curves of the devices with the BCP charge trapping layers stretched at tensile strain from 0 to 100%. The memory windows of A1-, B1-, and C1-based devices at 100% strain are 30, 60, and 76 V, respectively, and the I_{ON}/I_{OFF} ratios are as high as 10^6 (Figure S22). As shown in the OM images of Figure S19, A1 thin film only slightly cracks while B1 and C1 films are nearly intact under 100% strain. Therefore, the charges can still be effectively stored in the trapping layers under high strain and the memory windows are comparable to those of the corresponding unstrained films (36, 67, and 78 V in Table 2), especially for the star-shaped C1 film.

We also performed the stability tests of the devices with the BCP films that were stretched and released at 50% strain up to 1000 cycles. Figure 6 shows the memory window and the charge carrier mobility of A1-, B1-, and C1-based devices as functions of stretching/releasing cycle. For A1 thin film, the mobility sharply decreases by 1 order of magnitude and the memory window also decreases after 400 cycles. Remarkably, the mobilities and the memory windows keep nearly constant until 1000 cycles for B1 and C1 thin films.

Figure 7 and Figure S23 show the OM images of A1, B1, and C1 films with increasing stretch−release cycles at 50% strain. Microscale cracks are observed in A1 thin film at 50 cycles, and the number of the cracks greatly increases after 400 cycles, as indicated by the red circle, whereas B1 and C1 thin films reveal only a few cracks at 400 cycles and no significant increase in the number of cracks is found at 1000 cycles. Figure S24 shows the 1-D GISAXS profiles of A1 and B1 thin films along the q_y-axis after stretch−release tests at 50% strain for 0, 100, 400, and 1000 cycles. All the profiles of A1 and B1 films exhibit parallel HEX cylinders regardless of the number of the cycles. The d-spacing of the MH cylinders in A1 thin film is unchanged after 1000 cycles, and that in B1 thin film only slightly increases from 10.6 to 11.0 nm, suggesting that the microdomains can be maintained after the stretch−release cycles even though the macroscopic cracks have appeared.[36] Therefore, it is not the change of the BCP microdomains but rather the cracks of the films responsible for the decay of the electrical performance after cyclic stretching. Figure S25 shows the AFM surface morphologies of pentacene deposited on A1 and B1 films after stretch−release tests. For A1 film that cracks severely above 50 cycles, the grain size of top pentacene layer greatly decreases after the film is tested for 400 and 1000 cycles. In contrast, for B1 film that reveals fewer cracks, the

grain size of pentacene is not significantly changed with the cycles. Thus, the formation of the cracks in the trapping layer not only lowers the charge storage capability but also deteriorates the packing of the top semiconductor layer and causes a smaller grain size so that the charge transport is retarded due to an increase in the areas of grain boundary.

We have shown that a stable memory performance under stretching can be achieved by the use of the BCPs with MH and PBA segments as the charge trapping layers in the FET devices, especially for ABA-type and star-shaped BCP thin films. The plausible mechanism is discussed as follows. For the BCP films, the stretchability is imparted by the soft PBA chains that can move freely at room temperature. The hard MH domain plays two roles here. In addition to the role as the charge trapping sites, it also works as the junction that provides mechanical strength due to the strong molecular interaction between MH chains. For ABA-type and star-shaped BCPs, the multiple MH blocks in one BCP molecule may join in different MH domains, and the middle soft PBA blocks then become the tie chains connecting the hard domains, as illustrated in Figure 8. In other words, the hard MH domains serve as the physical cross-linking points linked by the soft PBA chains, similar to the structure of elastomers, which prevents the films from tearing apart under high, repeated strain. In the case of linear AB-type BCP, the PBA blocks are unable to work as tie chains between MH domains, and thus the soft PBA domains break as PBA chains disentangle at relatively low strain.

CONCLUSIONS

In this study, the intrinsically stretchable BCPs consisting MH and PBA blocks in linear AB-type, ABA-type, and star-shaped architectures were successfully synthesized by ATRP and click reaction. The BCP thin films show either parallel cylindrical MH domains or highly ordered spherical MH domains, depending on PBA volume fraction and the molecular architecture. The stretchability of the thin films can be significantly improved by introducing the flexible PBA segment into BCPs. For ABA-type and star-shaped architectures with end MH blocks, physical networks are formed in the BCPs where the hard MH domains serve as the physically cross-linked junctions and the flexible PBA blocks in the middle are the tie chains connecting the junctions. Such a network structure endows the thin films with rubber elasticity. The films can thus endure high strain and the FET memory devices with ABA-type and star-shaped BCP thin films as charge trapping layers show remarkably stable charge carrier mobilities and memory windows even when the trapping layers are under severe cyclic strain tests. This work demonstrates that the design of the molecular architectures provides BCPs a great potential to be applied in high-performance stretchable and wearable electronic devices.

ASSOCIATED CONTENT

Ⓢ Supporting Information

The Supporting Information is available free of charge on the ACS Publications website at DOI: 10.1021/acs.macromol.8b00874.

    Experimental sections and supplementary tables and figures (PDF)

AUTHOR INFORMATION

Corresponding Authors
*E-mail chenwc@ntu.edu.tw (W.-C.C.).
*E-mail satoh@eng.hokudai.ac.jp (T.S.).
*E-mail shtung@ntu.edu.tw (S.-H.T.).

ORCID 🔘
Takuya Isono: 0000-0003-3746-2084
Shih-Huang Tung: 0000-0002-6787-4955
Toshifumi Satoh: 0000-0001-5449-9642
Wen-Chang Chen: 0000-0003-3170-7220

Notes
The authors declare no competing financial interest.

REFERENCES

(1) Kaltenbrunner, M.; Sekitani, T.; Reeder, J.; Yokota, T.; Kuribara, K.; Tokuhara, T.; Drack, M.; Schwödiauer, R.; Graz, I.; Bauer-Gogonea, S.; Bauer, S.; Someya, T. An ultra-lightweight design for imperceptible plastic electronics. *Nature* **2013**, *499*, 458.

(2) Lee, Y.; Shin, M.; Thiyagarajan, K.; Jeong, U. Approaches to Stretchable Polymer Active Channels for Deformable Transistors. *Macromolecules* **2016**, *49* (2), 433−444.

(3) Fan, J. A.; Yeo, W.-H.; Su, Y.; Hattori, Y.; Lee, W.; Jung, S.-Y.; Zhang, Y.; Liu, Z.; Cheng, H.; Falgout, L.; Bajema, M.; Coleman, T.; Gregoire, D.; Larsen, R. J.; Huang, Y.; Rogers, J. A. Fractal design concepts for stretchable electronics. *Nat. Commun.* **2014**, *5*, 3266.

(4) Wang, S.; Xu, J.; Wang, W.; Wang, G.-J. N.; Rastak, R.; Molina-Lopez, F.; Chung, J. W.; Niu, S.; Feig, V. R.; Lopez, J.; Lei, T.; Kwon, S.-K.; Kim, Y.; Foudeh, A. M.; Ehrlich, A.; Gasperini, A.; Yun, Y.; Murmann, B.; Tok, J. B. H.; Bao, Z. Skin electronics from scalable fabrication of an intrinsically stretchable transistor array. *Nature* **2018**, *555*, 83.

(5) Fu, H.; Xu, S.; Xu, R.; Jiang, J.; Zhang, Y.; Rogers, J. A.; Huang, Y. Lateral buckling and mechanical stretchability of fractal interconnects partially bonded onto an elastomeric substrate. *Appl. Phys. Lett.* **2015**, *106* (9), 091902.

(6) Choi, S.; Park, J.; Hyun, W.; Kim, J.; Kim, J.; Lee, Y. B.; Song, C.; Hwang, H. J.; Kim, J. H.; Hyeon, T.; Kim, D.-H. Stretchable Heater Using Ligand-Exchanged Silver Nanowire Nanocomposite for Wearable Articular Thermotherapy. *ACS Nano* **2015**, *9* (6), 6626−6633.

(7) Lipomi, D. J.; Tee, B. C. K.; Vosgueritchian, M.; Bao, Z. Stretchable organic solar cells. *Adv. Mater.* **2011**, *23* (15), 1771−1775.

(8) Choi, D.; Kim, H.; Persson, N.; Chu, P.-H.; Chang, M.; Kang, J.-H.; Graham, S.; Reichmanis, E. Elastomer−Polymer Semiconductor Blends for High-Performance Stretchable Charge Transport Networks. *Chem. Mater.* **2016**, *28* (4), 1196−1204.

(9) Wen, H.-F.; Wu, H.-C.; Aimi, J.; Hung, C.-C.; Chiang, Y.-C.; Kuo, C.-C.; Chen, W.-C. Soft Poly(butyl acrylate) Side Chains toward Intrinsically Stretchable Polymeric Semiconductors for Field-Effect Transistor Applications. *Macromolecules* **2017**, *50* (13), 4982−4992.

(10) Wu, H.-C.; Benight, S. J.; Chortos, A.; Lee, W.-Y.; Mei, J.; To, J. W. F.; Lu, C.; He, M.; Tok, J. B. H.; Chen, W.-C.; Bao, Z. A Rapid and Facile Soft Contact Lamination Method: Evaluation of Polymer Semiconductors for Stretchable Transistors. *Chem. Mater.* **2014**, *26* (15), 4544−4551.

(11) Wu, H.-C.; Hung, C.-C.; Hong, C.-W.; Sun, H.-S.; Wang, J.-T.; Yamashita, G.; Higashihara, T.; Chen, W.-C. Isoindigo-Based Semiconducting Polymers Using Carbosilane Side Chains for High Performance Stretchable Field-Effect Transistors. *Macromolecules* **2016**, *49* (22), 8540−8548.

(12) Liang, J.; Li, L.; Chen, D.; Hajagos, T.; Ren, Z.; Chou, S.-Y.; Hu, W.; Pei, Q. Intrinsically stretchable and transparent thin-film transistors based on printable silver nanowires, carbon nanotubes and an elastomeric dielectric. *Nat. Commun.* **2015**, *6*, 7647.

(13) Oh, J. Y.; Rondeau-Gagné, S.; Chiu, Y.-C.; Chortos, A.; Lissel, F.; Wang, G.-J. N.; Schroeder, B. C.; Kurosawa, T.; Lopez, J.; Katsumata, T.; Xu, J.; Zhu, C.; Gu, X.; Bae, W.-G.; Kim, Y.; Jin, L.; Chung, J. W.; Tok, J. B. H.; Bao, Z. Intrinsically stretchable and healable semiconducting polymer for organic transistors. *Nature* **2016**, *539*, 411.

(14) Rao, Y.-L.; Chortos, A.; Pfattner, R.; Lissel, F.; Chiu, Y.-C.; Feig, V.; Xu, J.; Kurosawa, T.; Gu, X.; Wang, C.; He, M.; Chung, J. W.; Bao, Z. Stretchable Self-Healing Polymeric Dielectrics Cross-Linked Through Metal−Ligand Coordination. *J. Am. Chem. Soc.* **2016**, *138* (18), 6020−6027.

(15) Liang, J.; Li, L.; Niu, X.; Yu, Z.; Pei, Q. Elastomeric polymer light-emitting devices and displays. *Nat. Photonics* **2013**, *7*, 817.

(16) Vosgueritchian, M.; Tok, J. B. H.; Bao, Z. Stretchable LEDs: Light-emitting electronic skin. *Nat. Photonics* **2013**, *7*, 769.

(17) Yu, Z.; Niu, X.; Liu, Z.; Pei, Q. Intrinsically Stretchable Polymer Light-Emitting Devices Using Carbon Nanotube-Polymer Composite Electrodes. *Adv. Mater.* **2011**, *23* (34), 3989−3994.

(18) Hwang, B.-U.; Lee, J.-H.; Trung, T. Q.; Roh, E.; Kim, D.-I.; Kim, S.-W.; Lee, N.-E. Transparent Stretchable Self-Powered Patchable Sensor Platform with Ultrasensitive Recognition of Human Activities. *ACS Nano* **2015**, *9* (9), 8801−8810.

(19) Jung, S.; Hong, S.; Kim, J.; Lee, S.; Hyeon, T.; Lee, M.; Kim, D.-H. Wearable Fall Detector using Integrated Sensors and Energy Devices. *Sci. Rep.* **2015**, *5*, 17081.

(20) Amjadi, M.; Pichitpajongkit, A.; Lee, S.; Ryu, S.; Park, I. Highly Stretchable and Sensitive Strain Sensor Based on Silver Nanowire−Elastomer Nanocomposite. *ACS Nano* **2014**, *8* (5), 5154−5163.

(21) Hua, Q.; Sun, J.; Liu, H.; Bao, R.; Yu, R.; Zhai, J.; Pan, C.; Wang, Z. L. Skin-inspired highly stretchable and conformable matrix networks for multifunctional sensing. *Nat. Commun.* **2018**, *9* (1), 244.

(22) Chou, H.-H.; Nguyen, A.; Chortos, A.; To, J. W. F.; Lu, C.; Mei, J.; Kurosawa, T.; Bae, W.-G.; Tok, J. B. H.; Bao, Z. A chameleon-inspired stretchable electronic skin with interactive colour changing controlled by tactile sensing. *Nat. Commun.* **2015**, *6*, 8011.

(23) Wang, J.-T.; Saito, K.; Wu, H.-C.; Sun, H.-S.; Hung, C.-C.; Chen, Y.; Isono, T.; Kakuchi, T.; Satoh, T.; Chen, W.-C. High-performance stretchable resistive memories using donor−acceptor block copolymers with fluorene rods and pendent isoindigo coils. *NPG Asia Mater.* **2016**, *8*, e298.

(24) Xie, K.; Wei, B. Materials and structures for stretchable energy storage and conversion devices. *Adv. Mater.* **2014**, *26* (22), 3592−3617.

(25) Liu, W.; Chen, J.; Chen, Z.; Liu, K.; Zhou, G.; Sun, Y.; Song, M. S.; Bao, Z.; Cui, Y. *Adv. Ener. Mater.* **2017**, *7* (21), 1701076.

(26) Trung Tran, Q.; Lee, N. E. Recent Progress on Stretchable Electronic Devices with Intrinsically Stretchable Components. *Adv. Mater.* **2017**, *29* (3), 1603167.

(27) Trung, T. Q.; Lee, N.-E. Materials and devices for transparent stretchable electronics. *J. Mater. Chem. C* **2017**, *5* (9), 2202−2222.

(28) Xu, J.; Wang, S.; Wang, G.-J. N.; Zhu, C.; Luo, S.; Jin, L.; Gu, X.; Chen, S.; Feig, V. R.; To, J. W. F.; Rondeau-Gagné, S.; Park, J.; Schroeder, B. C.; Lu, C.; Oh, J. Y.; Wang, Y.; Kim, Y.-H.; Yan, H.; Sinclair, R.; Zhou, D.; Xue, G.; Murmann, B.; Linder, C.; Cai, W.; Tok, J. B. H.; Chung, J. W.; Bao, Z. Highly stretchable polymer semiconductor films through the nanoconfinement effect. *Science* **2017**, *355* (6320), 59.

(29) Ning, X.; Wang, H.; Yu, X.; Soares, J. A. N. T.; Yan, Z.; Nan, K.; Velarde, G.; Xue, Y.; Sun, R.; Dong, Q.; Luan, H.; Lee, C. M.; Chempakasseril, A.; Han, M.; Wang, Y.; Li, L.; Huang, Y.; Zhang, Y.; Rogers, J. A. 3D Tunable, Multiscale, and Multistable Vibrational Micro-Platforms Assembled by Compressive Buckling. *Adv. Funct. Mater.* **2017**, *27* (14), 1605914.

(30) Xu, S.; Yan, Z.; Jang, K.-I.; Huang, W.; Fu, H.; Kim, J.; Wei, Z.; Flavin, M.; McCracken, J.; Wang, R.; Badea, A.; Liu, Y.; Xiao, D.; Zhou, G.; Lee, J.; Chung, H. U.; Cheng, H.; Ren, W.; Banks, A.; Li, X.; Paik, U.; Nuzzo, R. G.; Huang, Y.; Zhang, Y.; Rogers, J. A. Assembly of micro/nanomaterials into complex, three-dimensional architectures by compressive buckling. *Science* **2015**, *347* (6218), 154.

(31) Liu, Y.; Yan, Z.; Lin, Q.; Guo, X.; Han, M.; Nan, K.; Hwang, K. C.; Huang, Y.; Zhang, Y.; Rogers, J. A. Rogers John, A. Guided Formation of 3D Helical Mesostructures by Mechanical Buckling: Analytical Modeling and Experimental Validation. *Adv. Funct. Mater.* **2016**, *26* (17), 2909−2918.

(32) Fu, H.; Nan, K.; Bai, W.; Huang, W.; Bai, K.; Lu, L.; Zhou, C.; Liu, Y.; Liu, F.; Wang, J.; Han, M.; Yan, Z.; Luan, H.; Zhang, Y.; Zhang, Y.; Zhao, J.; Cheng, X.; Li, M.; Lee, J. W.; Liu, Y.; Fang, D.; Li, X.; Huang, Y.; Zhang, Y.; Rogers, J. A. Morphable 3D mesostructures and microelectronic devices by multistable buckling mechanics. *Nat. Mater.* **2018**, *17* (3), 268−276.

(33) Wang, J.-T.; Takshima, S.; Wu, H.-C.; Shih, C.-C.; Isono, T.; Kakuchi, T.; Satoh, T.; Chen, W.-C. Stretchable Conjugated Rod−Coil Poly(3-hexylthiophene)-*block*- poly(butyl acrylate) Thin Films for Field Effect Transistor Applications. *Macromolecules* **2017**, *50* (4), 1442−1452.

(34) Chiu, Y.-C.; Otsuka, I.; Halila, S.; Borsali, R.; Chen, W.-C. High-Performance Nonvolatile Transistor Memories of Pentacence Using the Green Electrets of Sugar-based Block Copolymers and Their Supramolecules. *Adv. Funct. Mater.* **2014**, *24* (27), 4240−4249.

(35) Chiu, Y.-C.; Sun, H.-S.; Lee, W.-Y.; Halila, S.; Borsali, R.; Chen, W.-C. Oligosaccharide Carbohydrate Dielectrics toward High-Performance Non-volatile Transistor Memory Devices. *Adv. Mater.* **2015**, *27* (40), 6257−6264.

(36) Hung, C.-C.; Chiu, Y.-C.; Wu, H.-C.; Lu, C.; Bouilhac, C.; Otsuka, I.; Halila, S.; Borsali, R.; Tung, S. H.; Chen, W. C. Conception of Stretchable Resistive Memory Devices Based on Nanostructure-Controlled Carbohydrate-*block*-Polyisoprene Block Copolymers. *Adv. Funct. Mater.* **2017**, *27* (13), 1606161.

(37) Isono, T.; Ree, B. J.; Tajima, K.; Borsali, R.; Satoh, T. Highly Ordered Cylinder Morphologies with 10 nm Scale Periodicity in Biomass-Based Block Copolymers. *Macromolecules* **2018**, *51* (2), 428−437.

(38) Satoh, Y.; Miyachi, K.; Matsuno, H.; Isono, T.; Tajima, K.; Kakuchi, T.; Satoh, T. Synthesis of Well-Defined Amphiphilic Star-Block and Miktoarm Star Copolyethers via t-Bu-P4-Catalyzed Ring-Opening Polymerization of Glycidyl Ethers. *Macromolecules* **2016**, *49* (2), 499−509.

(39) Satoh, Y.; Matsuno, H.; Yamamoto, T.; Tajima, K.; Isono, T.; Satoh, T. Synthesis of Well-Defined Three- and Four-Armed Cage-Shaped Polymers via "Topological Conversion" from Trefoil- and Quatrefoil-Shaped Polymers. *Macromolecules* **2017**, *50* (1), 97−106.

(40) Otsuka, I.; Zhang, Y.; Isono, T.; Rochas, C.; Kakuchi, T.; Satoh, T.; Borsali, R. Sub-10 nm Scale Nanostructures in Self-Organized Linear Di- and Triblock Copolymers and Miktoarm Star Copolymers Consisting of Maltoheptaose and Polystyrene. *Macromolecules* **2015**, *48* (5), 1509−1517.

(41) Isono, T.; Otsuka, I.; Suemasa, D.; Rochas, C.; Satoh, T.; Borsali, R.; Kakuchi, T. Synthesis, Self-Assembly, and Thermal Caramelization of Maltoheptaose-Conjugated Polycaprolactones Leading to Spherical, Cylindrical, and Lamellar Morphologies. *Macromolecules* **2013**, *46* (22), 8932−8940.

(42) Zhang, J.; Schneiderman, D. K.; Li, T.; Hillmyer, M. A.; Bates, F. S. Design of Graft Block Polymer Thermoplastics. *Macromolecules* **2016**, *49* (23), 9108−9118.

(43) Burns, A. B.; Register, R. A. Mechanical Properties of Star Block Polymer Thermoplastic Elastomers with Glassy and Crystalline End Blocks. *Macromolecules* **2016**, *49* (24), 9521−9530.

(44) Fetters, L. J.; Kiss, A. D.; Pearson, D. S.; Quack, G. F.; Vitus, F. J. Rheological behavior of star-shaped polymers. *Macromolecules* **1993**, *26* (4), 647−654.

(45) Pearson, D. S.; Helfand, E. Viscoelastic properties of star-shaped polymers. *Macromolecules* **1984**, *17* (4), 888−895.

(46) Müller, M.; Schick, M. Ordered Phases in Rod−Coil Diblock Copolymers. *Macromolecules* **1996**, *29* (27), 8900−8903.

(47) Pickett, G. T.; Balazs, A. C. Equilibrium Orientation of Confined Diblock Copolymer Films. *Macromolecules* **1997**, *30* (10), 3097−3103.

(48) Matsen, M. W.; Mahmoudi. Segregation of chain ends to the surface of a polymer melt. *Eur. Phys. J. E: Soft Matter Biol. Phys.* **2014**, *37* (8), 78.